Solar Phys
DOI 10.1007/s11207-013-0295-7

Rapid Formation and Disappearance of a Filament Barb

Anand D. Joshi · Nandita Srivastava · Shibu K. Mathew · Sara F. Martin

Received: 22 May 2012 / Accepted: 2 April 2013

Abstract We present observations of an activated quiescent filament obtained in Hα from the high-resolution *Dutch Open Telescope* (DOT) on 20 August 2010. The filament developed a barb in 10 min, which disappeared within the next 35 min. A data set from the DOT spanning 2 h was used to analyse this event. Line-of-sight velocity maps were constructed from the Doppler images, which reveal flows in filament spine during this period. Photospheric magnetograms were used from the *Helioseismic and Magnetic Imager* (HMI) on board the *Solar Dynamics Observatory* (SDO) to determine the changes in magnetic flux in the region surrounding the barb location. The analysis shows flows in the filament spine towards the barb location preceding its formation, and flows in the barb towards the spine during its disappearance. Magnetograms reveal patches of minority polarity flux close to the end of the barb at its greatest elongation. The flows in the spine and barbs are along numerous threads that compose these typical filament structures. The flows are consistent with field-aligned threads and demonstrate that the replacement time of the mass in barbs, and by inference, in the spine is very rapid.

Keywords Filament, disappearance · Filament, quiescent · Magnetic field

1. Introduction

Solar filaments are structures with high density and low temperature found in the chromosphere and low corona. They appear dark when seen against the solar disc, and bright

A.D. Joshi (✉) · N. Srivastava · S.K. Mathew
Udaipur Solar Observatory, Physical Research Laboratory, P.O. Box 198, Badi Road, Udaipur 313001, India
e-mail: janandd@prl.res.in

A.D. Joshi
Korea Astronomy and Space Science Institute, 776 Daedeokdae-ro, Yuseong-gu, Daejeon 305 348, Republic of Korea

S.F. Martin
Helio Research, 5212 Maryland Avenue, La Crescenta, CA, USA

Published online: 02 May 2013

when seen against the limb in chromospheric lines. Filaments are typically long-lived features, their lifetime ranging from about a day to several weeks. However, the basic building blocks of filaments are fine threads of streaming mass (Engvold, 1998; Lin, 2004; Lin *et al.*, 2005a). At the highest spatial resolution of observations today, the threads are short-lived and traceable for minutes (Engvold, 2004; Lin, Martin, and Engvold, 2008). From time-lapse movies of prominences and filaments that have been available since the 1950s, it is well known that filaments are highly dynamic, even in their most quiet states. In a non-perturbed state, the normal motion in the main part of filaments is counter-streaming within the fine and nearly parallel thread structure throughout the major parts of filaments and prominences (Schmieder, Raadu, and Wiik, 1991; Zirker, Engvold, and Martin, 1998; Berger *et al.*, 2010; Schmieder *et al.*, 2010).

Frequently, filaments are qualitatively classified as active region, intermediate, and quiescent according to their association with magnetic fields of high, medium, and low flux density, respectively. Indeed, Anderson and Martin (2005) studied a single long filament that spanned regions of high, intermediate, and low magnetic flux densities. On the other hand, physically meaningful classifications of filaments can be established by showing different mechanisms of formation, patterns of mass flows, or significantly different structure. Examples are filaments whose structure, in a non-activated condition, is characterised by counter-streaming throughout their spines and barbs. In contrast are the less common 'coronal cloud prominences' which do not have spines and barbs and exhibit only thin streams of down-flowing mass similar to coronal rain, instead of counter-streaming (Liu, Berger, and Low, 2012). The example in this paper is one that belongs to the most common class of filaments as discussed in the review articles by Labrosse *et al.* (2010), Mackay *et al.* (2010), and Lin (2011).

As their category implies, filaments with spines and/or barbs are grouped together because of the close relationship between these two primary structures which are both composed of fine threads. Filaments can have a spine without barbs but barbs do not exist without a spine. However, a spine can be invisible in Hα due to its low density but visible in 304 Å images. Filament spines are found along the zones between areas of oppositely directed photospheric magnetic fields, known variously as a neutral line, polarity inversion line (PIL), or polarity reversal boundary (Martin 1973, 2003). The spine consists of a thin sheet of threads that can extend over the entire length of a filament or a long section of it. The spine is typically confined to a narrow ribbon of plasma directly above the polarity reversal boundary, with the exception that the ends may splay out to join adjacent points in the chromosphere. The barb threads have one end in the spine and another end that veers outward and downward to the side of the spine. The orientation of the threads of barbs relative to the spine can be used to assign chirality to the filament, which can be either dextral or sinistral (Martin, Bilimoria, and Tracadas, 1994; Martin, 2003).

There is uncertainty regarding the rooting of barbs relative to the photospheric magnetic structure. The question is whether barbs are rooted in or precisely between the major and minor polarities present on either side of a filament. Initially, Martin (1998) discussed this question and gave evidence indicating that a barb is rooted in small-scale fields of parasitic or minor polarity, *i.e.* the polarity opposite to the dominant photospheric polarity adjacent to the filament. Rooting in the minor polarity would be consistent with field directions determined from chiral properties of filament channels and filaments. However, observations have not yet confirmed this deduction, and it has been suggested from the data taken at Big Bear Solar Observatory that barbs terminate not in minor polarities, but in polarity reversal boundaries that divide magnetic elements of minor polarity from those of major polarity (Chae, Moon,

and Park, 2005). Also, Lin *et al.* (2005b) have shown, using observations from the National Solar Observatory at Sacramento Peak and Swedish 1-m Solar Telescope, that 65 % of the barbs that they analysed terminate in the photospheric network boundaries. Although their magnetic field observations were relatively insensitive to intra-network magnetic fields, the boundaries of network magnetic fields are also sites at or close to pockets of small-scale intra-network magnetic fields of opposite polarity. Distinguishing between these subtle differences in the rooting of the barbs requires magnetic field and Hα wing observations of at least sub-arcsecond spatial resolution, and also magnetograms having good sensitivity to intra-network magnetic fields.

Aulanier and Demoulin (1998) proposed a theoretical model known as the 'dip model' of prominences, where the barb is supported by means of a dip in the magnetic field lines over minor polarity. Along similar lines, van Ballegooijen (2004) used the magnetic dips to model observed filament barbs. Indeed, López Ariste *et al.* (2006) observed the bald patches or dips using vector magnetic field measurements over the parasitic polarities at the footpoints of barbs. However, Karpen *et al.* (2001) have shown that the magnetic dips are a non-essential feature, as long as the fine structure of a prominence undergoes continuous evolution. Aulanier *et al.* (1999) and more recently Liu, Xu, and Wang (2010) have shown that the direction of barbs may evolve in response to magnetic flux emerging from the photosphere. Based on observations, Engvold (1998) suggested that barbs might be essential for the formation and existence of quiescent prominences; many active region filaments can be found without barbs.

An important aspect pertaining to the evolution of filaments is the flows in the surrounding photosphere. Martin (1990) suggested converging flows leading to cancelling magnetic fields as necessary conditions for the formation and maintenance of filaments. van Ballegooijen and Martens (1989) and Ridgway and Priest (1993) have shown converging photospheric flows to be responsible for the sheared configuration of magnetic fields in the region surrounding a filament. However, Magara and Kitai (1999) have found not only converging, but random flows in the photosphere in the vicinity of a filament. More recently, Rondi *et al.* (2007) have found diverging photospheric flows before and after a filament eruption. Several studies on the velocities in prominences using observations in Hα and extreme ultra-violet, are summarised by Labrosse *et al.* (2010) and Mackay *et al.* (2010). The typical range of plane-of-sky and line-of-sight (LOS) velocities is from 5 to 30 $\mathrm{km\,s^{-1}}$.

In order to study the possible role played by barbs in providing stability to filaments, we carried out high resolution observations from the *Dutch Open Telescope* (DOT) in August 2010. In this paper we present observations and analysis of a barb of a quiescent filament showing activations recorded on 20 August 2010 from the DOT. As the filament erupted a few days later, the analysis presented here assumes significance in understanding the repeated activations of a filament preceding its eruption.

2. Observations and Analysis

A filament, located approximately at 37° E, 32° S, near NOAA active region (AR) 11100 was observed in Hα from 19 to 27 August 2010 using the DOT situated at La Palma, Spain (Rutten *et al.*, 2004). The filament extended from within the AR to the quiet Sun region south of the AR. From the time-lapse sequence of images taken at the DOT, we observed the filament underwent a lot of changes in its shape, before ultimately erupting on 27 August 2010 when it appeared just above the west limb of the Sun. Because the part of this filament, observed from the DOT, lay outside the AR amidst fields of very low magnetic flux density, we classified this part as belonging to the quiescent category.

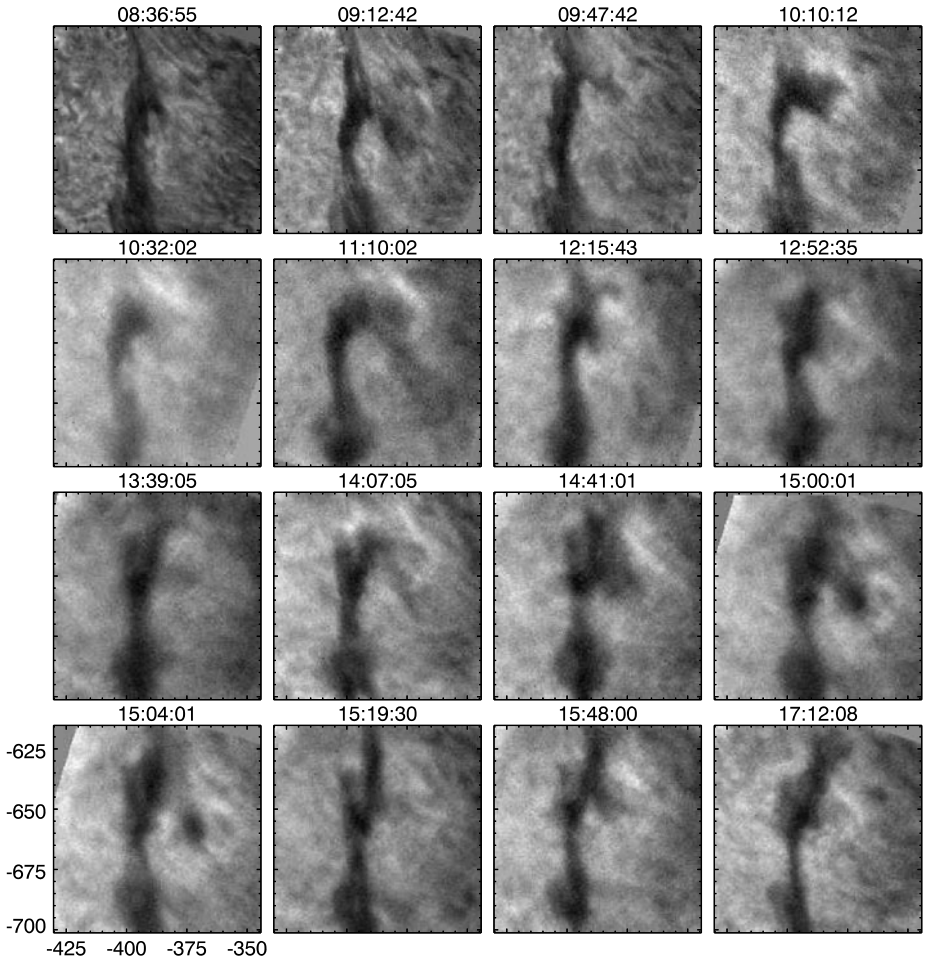

Figure 1 A series of Hα line centre images from DOT on 20 August 2010. The images show the formation and disappearance of a filament barb several times in a span of 11 h. The first formation and disappearance observed is studied in detail because the atmospheric distortions to the image were least in the early morning at the DOT, while the overall evolution throughout the day calls attention to the short-lived nature of the barb.

On 20 August 2010 the northern end of the filament showed at least four instances of rapid formation and disappearance of a barb on the same side of the filament and at approximately the same location. Such a rapid formation and disappearance of a barb is neither well-known nor widely reported. This prompted us to study this event in detail. A series of the Hα line centre images is shown in Figure 1, wherein the barb can be seen to be forming and disappearing. The lifetime of the barb in each instance is only a few tens of minutes.

The seeing at the DOT was good in the first 2 h of observations, from 08:00 to 10:00 UT, and deteriorated rapidly during the day. Hence, we present in detail the barb that was visible from 09:00 to 09:45 UT. Speckle reconstruction of images was carried out over the initial 2-h interval, which were used for the present analysis (Keller and von der Lühe, 1992; Sütterlin *et al.*, 2001b). Images for this event were recorded in seven positions across the Hα line at $\Delta\lambda$ equal to 0.0 Å, ± 0.3 Å, ± 0.6 Å, and ± 0.9 Å. The observations of the barb

presented here extend from 08:00 UT until 09:55 UT on 20 August 2010, with a cadence of 30 s.

2.1. Analysis Techniques for DOT Image

We briefly describe the analysis techniques, namely the offline technique for image restoration, and a method to determine the LOS velocity from Hα Doppler images. The small field-of-view (FOV) of the DOT meant that even tiny errors in telescope tracking produced significant motion between consecutive images. To rectify this, cross correlations were determined between consecutive pairs of images, and the images were shifted accordingly. This process was repeated for all the images in all line positions. On running the sets of aligned images in the form of a time-lapse movie, it was possible to observe changes in the structure of the filament and the barb.

2.1.1. Speckle Reconstruction

At the DOT, a total of 140 images, known as a burst, were recorded in the continuum near Hα line within a time interval of 30 s. The broad-band speckle reconstruction method as described in Keller and von der Lühe (1992) was used to reconstruct these continuum images. During the same time, 20 images were recorded in each of the seven line positions along the Hα spectral line, thus scanning the line in the same time as the 140 continuum images. The optical transfer function obtained for the continuum was then applied to the seven sets of images, each containing 20 images at a given line position, to obtain the reconstructed images at each position (Keller and von der Lühe, 1992; Sütterlin, Rutten, and Skomorovsky, 2001a). This method is very effective since it does not compromise the reconstructed image quality, and allows us to scan the entire Hα line in a small time interval of 30 s.

2.1.2. Line-of-Sight Velocity Maps

High resolution observations taken in the chromospheric Hα line reveal a great deal of fine structure in filaments. However, motion of the filament along the line-of-sight (LOS) induces Doppler shift in the spectral line, rendering the filament invisible in the line centre if the LOS motion is sufficiently large. For the purpose of recording Doppler shifts, images are taken at several positions along the Hα line by an automated rotation of the calcite stages of a tunable Lyot filter at the DOT. In the past, Engvold and Malville (1977) and Martres *et al.* (1981) have used the spectroscopic measurements across the Hα line to determine velocities in prominences.

To determine the LOS velocity, we have adopted the method given in Lin (2004). The Hα line is first fitted with a Gaussian function of the form:

$$I = I_0 e^{-\tau(\Delta\lambda)} \tag{1}$$

where I_0 is the Hα continuum, and the line absorption is given by

$$\tau(\Delta\lambda) = \tau_0 \exp\left[-\left(\frac{\Delta\lambda_{\rm ls} + \Delta\lambda}{\Delta\lambda_{\rm D}} \right)^2 \right]. \tag{2}$$

In the above equation, τ_0 is the optical depth at line centre, and $\Delta\lambda_{\rm D}$ is the Doppler width of the profile. The line shift, $\Delta\lambda_{\rm ls}$, is determined by taking images at $\lambda_0 - \Delta\lambda$, λ_0, and $\lambda_0 + \Delta\lambda$.

From Equation (2), the intensities of images at these three positions, denoted, respectively, by I_-, $I_{\rm lc}$, and I_+, are

$$I_- = I_0 \exp\left[-\tau_0 e^{-\left(\frac{\Delta\lambda_{\rm ls}-(\lambda_0-\lambda)}{\Delta\lambda_{\rm D}}\right)^2}\right], \tag{3}$$

$$I_{\rm lc} = I_0 \exp\left[-\tau_0 e^{-\left(\frac{\Delta\lambda_{\rm ls}}{\Delta\lambda_{\rm D}}\right)^2}\right], \quad \text{and} \tag{4}$$

$$I_+ = I_0 \exp\left[-\tau_0 e^{-\left(\frac{\Delta\lambda_{\rm ls}+(\lambda_0-\lambda)}{\Delta\lambda_{\rm D}}\right)^2}\right]. \tag{5}$$

On combining the three equations above, τ_0 and $\Delta\lambda_{\rm D}$ are eliminated (Lin, 2004) to give

$$\Delta\lambda_{\rm ls} = \frac{\Delta\lambda(1-A)}{2(1+A)} \tag{6}$$

where A is defined as

$$A = \frac{\log\left(\frac{\log I_0 - \log I_-}{\log I_0 - \log I_{\rm lc}}\right)}{\log\left(\frac{\log I_0 - \log I_+}{\log I_0 - \log I_{\rm lc}}\right)}. \tag{7}$$

Here, $I_{\rm lc}$, I_+, and I_- are the intensities at λ_0, $\lambda_0+\Delta\lambda$, and $\lambda_0-\Delta\lambda$, while I_0 is the continuum intensity. Once $\Delta\lambda_{\rm ls}$ is obtained, the LOS velocity is

$$v_{\rm los} = c\frac{\Delta\lambda_{\rm ls}}{\lambda_0} = \frac{c}{\lambda_0}\frac{\Delta\lambda(1-A)}{2(1+A)}. \tag{8}$$

The images during our observing run at the DOT were sequentially captured at Hα line centre, and at $\Delta\lambda$ equal to ± 0.3 Å, ± 0.6 Å, and ± 0.9 Å from the line centre.

From Equation (6), we find that the continuum intensity, I_0, is also needed to determine the LOS velocity in Equation (8). A Gaussian is fitted to the intensities in the seven line positions for a given time to regenerate the Hα line profile. From the BASS2000 Solar Survey Archive, we find the full-width at half-maximum (FWHM) of the Hα line to be 1.44 Å. The Hα continuum is twice the intensity at which the fitted Gaussian function has its width equal to FWHM. The continuum is determined for a small region of the chromosphere for each time of the observation. I_0 for a given time is then determined by taking the average over this region.

To construct a LOS velocity map we need three images, one in line centre, and one each in the red and blue wings. As we have images in seven line positions, three different LOS velocity maps could be constructed. Of these three maps, since images at ± 0.3 Å are too close to the line centre image, the changes in intensity were not significant enough to visually see the LOS velocity. Also, the images at ± 0.9 Å were found to be too far away from the line centre image to detect changes in the structure. Therefore, we present the results obtained from the LOS velocity maps constructed using images at line centre and at ± 0.6 Å.

2.2. HMI Observations

In addition to line centre images and LOS velocity maps, we also analysed changes in magnetograms obtained from the *Helioseismic and Magnetic Imager* (HMI: Scherrer *et al.*, 2011) on board the *Solar Dynamics Observatory* (SDO: Pesnell, Thompson, and Chamberlin, 2011), in order to study the role of magnetic fields. We used full-disc Hα images

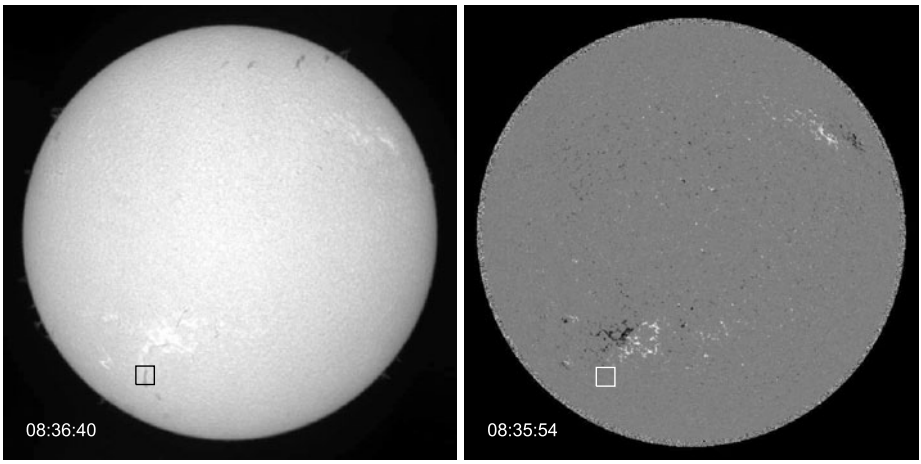

Figure 2 Full-disc Hα image from KSO (left) and LOS magnetogram from HMI/SDO (right) for 20 August 2010. The field-of-view of the DOT is marked on both images using a square.

from Kanzelhöhe Solar Observatory (KSO) as an intermediate step to co-align HMI magnetograms with DOT images. A feature in the DOT line centre image that could be seen even in moderate resolution was identified in the full-disc image from KSO. By taking into account the size of the DOT field-of-view (FOV) determined from its plate scale, a region of interest (ROI) was selected from the KSO FOV such that coordinates of the feature in this ROI were the same as in the DOT FOV. To make sure that the correct KSO ROI was selected, the KSO FOV was overlaid with contours of DOT Hα line centre image.

The (x, y) coordinates of this ROI are from $(-430, -701)$ to $(-345, -616)$ in arcsec with respect to the disc centre. The ROI is marked on the Hα image from the DOT and HMI LOS magnetogram in Figure 2. These coordinates were then used to extract the corresponding ROI from full-disc HMI images. Thus, we could overlay the HMI contours on top of DOT images to study simultaneous changes in LOS magnetic field. The filament under study had very weak photospheric magnetic field surrounding it. Hence, to build up the signal and reduce noise, we made use of an average of three consecutive HMI LOS magnetograms taken at a cadence of 45 s. Examples of the resulting contours are shown in the first column of Figure 3 overlaid on Hα images. These coordinates were then converted into heliographic coordinates, and the corresponding ROI from full-disc HMI images was extracted. Thus, we could overlay the HMI contours on top of DOT images to study simultaneous changes in LOS magnetic field. To build up the signal and reduce noise, we made use of an average of three consecutive HMI LOS magnetograms taken at a cadence of 45 s.

3. Results and Discussion

3.1. Formation and Disappearance of Barb

The observation of the filament started at 08:00 UT. The line centre images did not show significant changes until almost 09:00 UT. Between 09:00 and 09:11 UT, observations had to be suspended to carry out the routine task of getting dark and flat frames, and refocusing the telescope. On resuming observations at 09:11 UT, a barb was observed to have formed

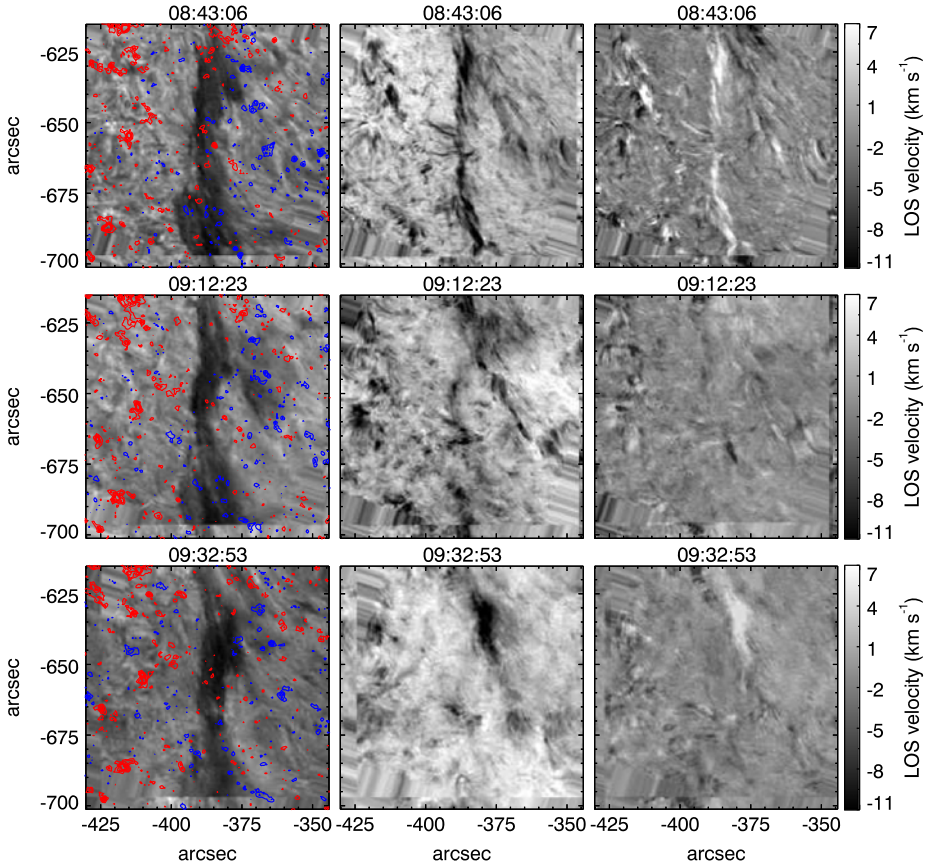

Figure 3 A series of images used to study the filament barb on 20 August 2010. Left: Overlay of LOS magnetograms from HMI/SDO on Hα line centre images from the DOT. Blue indicates positive polarity, and red indicates negative, with the contours drawn at $\pm 20, \pm 40, \pm 60, \pm 80$, and ± 100 G. Middle: Images in blue wing of Hα at $\Delta\lambda = -0.6$ Å. Right: LOS velocity maps created from Hα line centre, and ± 0.6 Å images. The colour bar at the right shows that white (+) is toward the observer and black (−) is away from the observer. The time for each image is shown at the top. All the axis coordinates are in terms of arcsec from the Sun centre.

at the northern end of the DOT FOV as can be seen in Figure 3. Thus, we infer that the barb formed sometime within a short span of 11 min from 09:00 to 09:11 UT. The formation of a barb could also be seen in the low resolution observations from full-disc KSO images. The barb remained more or less unchanged until about 09:26 UT, after which it started to disappear, and could no longer be seen in the line centre images at 09:45 UT.

Images before and after the formation a filament barb are shown at three different times in Figure 3. The first column consists of a series of Hα line centre image superposed with LOS magnetic field contours. The middle column shows images in the blue wing of Hα at $\Delta\lambda = -0.6$ Å, while the right column shows LOS velocity maps. The contours on line centre images in the left column show positive polarity in blue and negative in red, with the contours drawn at $\pm 20, \pm 40, \pm 60, \pm 80$, and ± 100 G (gauss). In the blue wing images in the middle column, blue-shifts could be seen as dark regions moving along the spine and barb. However, to determine the actual line shift responsible for this, and consequently the

LOS component of the velocity, we have used Equations (6) and (8). In the right column showing the LOS velocity we have restricted the colour bar from -11 to 7 km s^{-1} in order to increase the visibility of the flows. In some of the images though, the LOS velocity has exceeded these limits.

In Figure 3, images in the left and middle columns are shown to be taken at the same time. This is because the information obtained from the header of the file is for the entire burst, and not for each position individually. In reality, images taken in the two line positions are separated by about 12 s. The three HMI magnetograms used for making an average are such that the time of the middle one is closest to the time for a given DOT image.

3.2. Flows Accompanying Barb Disappearance

The right column in Figure 3 shows LOS velocity maps produced using a line centre image, and images at ± 0.6 Å. We observe that there is no LOS velocity seen until 08:30 UT. After this and until 08:58 UT, we could observe blue-shifts along the filament spine with LOS velocity up to ≈ 15 km s^{-1}, as seen in the LOS velocity image at 08:43:06 UT in Figure 3. Compared to such relatively high values of velocity in the spine, the surrounding chromosphere showed very small values of ≈ 1 km s^{-1}. Before the barb formation, red-shifts were observed from 08:50 to 09:00 UT going from the spine to the barb. Later, during the disappearance of the barb, blue-shifts were observed in the spine from 09:26 to 09:40 UT going towards the location where the barb joined the filament spine, as seen in the LOS velocity image at 09:32:53 UT in Figure 3.

The features observed to have a LOS component of velocity were also seen to move in the plane of sky towards the location where the barb connected with the spine. We term such features as moving velocity features (MVFs). MVFs need not necessarily be mass flows, as adjacent parts of the spine could show a LOS velocity component in response to a wave passing through the spine, owing to which there appears a moving LOS component of the velocity. To rule out this possibility, time-lapse movies in Hα line centre were studied carefully, wherein moving blobs within the filament spine could be observed. We therefore interpret the MVFs to be plane-of-sky components of the actual mass flows in the filament spine.

Two MVFs were followed in different parts of the filament spine. One MVF observed from 08:30 to 08:40 UT in the lower half of the FOV had a plane-of-sky velocity component of 18 km s^{-1}, whereas another MVF observed in the upper half of the FOV from 08:39 to 08:46 UT had a plane-of-sky velocity component of 31 km s^{-1}.

From 08:51 to 09:00 UT we can see red-shift reaching up to 11 km s^{-1} at the point where the barb connected with the spine. We suggest that this is the mass flowing downward that forms the barb, which initially we can see only in the LOS velocity maps, but not in the line centre images. It is only from 09:24 UT onward, *i.e.* just before the barb starts to disappear, that we see blue-shifts in the barb. We find MVFs in the barb too, just like in the spine. One of the MVFs tracked in the barb from 09:24 to 09:30 UT showed a plane-of-sky velocity component of 38 km s^{-1} and it moved from the barb footpoint towards the spine. These MVFs in the barb could be observed until 09:42 UT. The sequence of events is given in Table 1. Changes in the magnetic field around the barb are shown in Figure 4 as described in the following section.

3.3. Magnetic Flux Variation

The filament was seen to lie along the polarity reversal boundary with the negative field dominant on the east side of the filament, and positive field dominant on the west side.

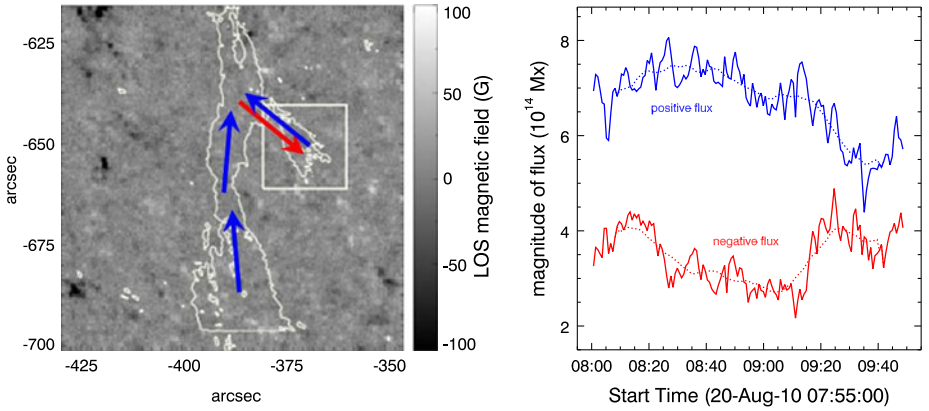

Figure 4 Left: HMI LOS magnetogram overlaid with the contours of filament and barb outline. The white square marks the region surrounding the barb location over which flux is calculated. The red and blue arrows indicate, respectively, the location of the blue-shifts and red-shifts. Right: The positive (blue) and negative (red) flux in the region inside the white square.

Table 1 Summary of the temporal evolution of rapidly forming and disappearing barb and the changes in filament structure before and after.

Time (UT)	Observational remarks
08:31 – 08:55	Blue-shifts in spine, ≥ 11 km s^{-1} (mass flow towards barb)
08:36 – 08:59	Strong red-shifts at top of barb, ≈ 10 km s^{-1} (mass flows leading to barb formation)
09:00 – 09:11	Formation of barb in Hα line centre
09:00 – 09:35	Decrease of positive flux around barb location
09:25 – 09:45	Barb disappears in Hα line centre
09:25 – 09:40	Strong blue-shifts in barb, ≥ 10 km s^{-1} (mass flows towards spine)

The barb appeared on the west side of the filament spine, and there is little change in the magnetic field on the east side of the spine. The west side showed three concentrations of the dominant (positive) magnetic field at the location of the barb. We have selected an area of $21'' \times 21''$ covering the area of the barb and calculated the total positive and negative flux in this region. Figure 4 (left panel) shows the HMI ROI wherein the white square identifies the area within which the positive and negative magnetic fluxes were calculated. The locations of blue-shifts and red-shifts are indicated as blue and red arrows in the figure. Changes in the positive and negative fluxes within the white square are shown in the right panel.

From this figure, we observe that in the region surrounding the barb footpoint, positive flux is always more than the negative flux, which is expected since the former is the dominant polarity. From 08:00 UT until about 09:00 UT we find that both the positive and negative fluxes remain more or less constant. As the barb starts to appear at 09:00 UT, the positive flux decreases until 09:35 UT. Once the barb is formed by 09:11 UT, the negative polarity shows a sharp increase. This shows that although the barb site is populated with dominant polarity before its formation, once the barb appears, the strength of dominant polarity decreases.

To verify how significant the changes in magnetic flux are, we determined the magnetic flux in exactly the same area as the white square in a quiet region that is as distant from the Sun centre as the region in the DOT FOV. The background positive and negative fluxes

were almost constant in magnitude at 4×10^{14} Mx (maxwell). This is almost the same in magnitude as the negative flux shown in Figure 4 (right panel). This indicates that although the barb site is populated with dominant polarity before its formation, once it appears the strength of dominant polarity decreases. Therefore, we cannot claim significance of the observed magnitude of changes in negative flux in Figure 4 during the same time because they are similar in magnitude to other background fluctuations away from the filament. It remains an open question as to whether ordinary changes in the network can affect the structure of a nearby filament.

4. Summary

The high resolution observations of an activated quiescent filament in Hα line centre and Dopplergrams from DOT, complemented with near-simultaneous high resolution magnetograms of the same region from HMI/SDO, are presented in this paper. This provided us an opportunity to understand the rapid formation and disappearance of a barb of an activated quiescent filament on 20 August 2010. As the filament erupted later, on 27 August 2010, when it was on the western limb, it is desirable to point out the importance of such studies of barb stability and their dynamic evolution.

Based on the high resolution observations from the DOT and the HMI described above, we summarise in Table 1 the overall picture of formation and disappearance of the barb, and the changes taking place in the filament before and after the barb formation and its subsequent rapid disappearance.

The results of our analysis provide evidence that mass flow from the spine led to barb formation. This can be seen first from the discrete velocity features moving towards the barb location, with average plane-of-sky speeds ≈ 25 km s^{-1}, and later from red-shifts at the place where the barb appears to connect with the spine. The barb was next seen fully formed after an 11-min gap in the observations. Moving velocity features were also observed during the disappearance of the barb, with plane-of-sky speeds ≥ 30 km s^{-1}, moving upward along the barb to the location where it smoothly merges with the spine.

The filament was located at 37° E, 32° S, which is about 47° S from the disc centre. Thus, the observed blue-shifts can be interpreted as the LOS components of flows in the spine travelling towards north, and the red-shifts as flows travelling southwards. Similarly the MVFs observed can also be interpreted as plane-of-sky components of the same flows. If we consider the blue-shift component to be 10 km s^{-1} along the line-of-sight, and MVF component to be 25 km s^{-1} in the plane of the sky, then the velocity of flow in the filament spine would be approximately 27 km s^{-1}. This is based on the assumption that the filament velocity has no local vertical component. Since the filament more or less maintained its shape throughout the day, this is a valid assumption.

The new barb appeared on the west side of the filament spine where positive polarity was dominant. From the flux calculated using HMI magnetograms, we observe that the barb formation was accompanied with decreasing positive flux. However, owing to the small amplitude of concurrently decreasing and then increasing negative magnetic flux, we are unable to verify with certainty its role in the barb formation and disappearance.

5. Conclusions

From analysing the mass flow present in a filament observed at the Dutch Open Telescope, we have learned that filament barbs can develop quickly from mass motions along the spine

that become redirected to the chromosphere at the side of the prominence. Barbs can also disappear by retraction or return of their mass upward into the spine. The appearance or disappearance can happen in a short span of the order of a few tens of minutes.

Acknowledgements This paper was possible in part by funding for the DOT prominence project through (a) US National Science Foundation (NSF) grant AGS-1024793 to Helio Research and (b) supporting US NSF grants AGS-0837915 and AGS-0852249 to Helio Research for specific studies by the PROM research team. The authors are grateful to the staff at the *Dutch Open Telescope*, namely Rob Hammerschlag, Guus Sliepen and Felix Bettonvil, for providing invaluable assistance during observations. The authors also acknowledge Brittany McCrigler who has kindly carried out the speckle reconstruction of the DOT data analysed in this paper. We thank the HMI/SDO team for providing the valuable data. The HMI data are downloaded via the Virtual Solar Observatory and the Joint Science Operations Center. The full-disc Hα images from the Kanzelhöhe Solar Observatory, Austria, are courtesy of the Central European Solar ARchives.

References

Anderson, M., Martin, S.F.: 2005, In: Sankarasubramanian, K., Penn, M., Pevtsov, A. (eds.) *Large-Scale Structures and Their Role in Solar Activity*, *ASP Conf. Ser.* **346**, 201.

Aulanier, G., Demoulin, P.: 1998, *Astron. Astrophys.* **329**, 1125.

Aulanier, G., Démoulin, P., Mein, N., van Driel-Gesztelyi, L., Mein, P., Schmieder, B.: 1999, *Astron. Astrophys.* **342**, 867.

Berger, T.E., Slater, G., Hurlburt, N., Shine, R., Tarbell, T., Title, A., Lites, B.W., Okamoto, T.J., Ichimoto, K., Katsukawa, Y., Magara, T., Suematsu, Y., Shimizu, T.: 2010, *Astrophys. J.* **716**, 1288. doi:10.1088/0004-637X/716/2/1288.

Chae, J., Moon, Y.-J., Park, Y.-D.: 2005, *Astrophys. J.* **626**, 574. doi:10.1086/429797.

Engvold, O.: 1998, In: Webb, D.F., Schmieder, B., Rust, D.M. (eds.) *New Perspectives on Solar Prominences*, *IAU Colloq.* **167**, 23.

Engvold, O.: 2004, In: Stepanov, A.V., Benevolenskaya, E.E., Kosovichev, A.G. (eds.) *Multi-Wavelength Investigations of Solar Activity*, *IAU Symp.* **223**, 187. doi:10.1017/S1743921304005575.

Engvold, O., Malville, J.M.: 1977, *Solar Phys.* **52**, 369. doi:10.1007/BF00149653.

Karpen, J.T., Antiochos, S.K., Mohensee, M., Klimchuk, J.A., MacNeice, P.J.: 2001, *Astrophys. J. Lett.* **553**, L85. doi:10.1086/320497.

Keller, C.U., von der Lühe, O.: 1992, *Astron. Astrophys.* **261**, 321.

Labrosse, N., Heinzel, P., Vial, J.-C., Kucera, T., Parenti, S., Gunár, S., Schmieder, B., Kilper, G.: 2010, *Space Sci. Rev.* **151**, 243. doi:10.1007/s11214-010-9630-6.

Lin, Y.: 2004, Magnetic field topology inferred from studies of fine threads in solar filaments. PhD thesis, University of Oslo.

Lin, Y.: 2011, *Space Sci. Rev.* **158**, 237. doi:10.1007/s11214-010-9672-9.

Lin, Y., Martin, S.F., Engvold, O.: 2008, In: Howe, R., Komm, R.W., Balasubramaniam, K.S., Petrie, G.J.D. (eds.) *Subsurface and Atmospheric Influences on Solar Activity*, *ASP Conf. Ser.* **383**, 235.

Lin, Y., Engvold, O., Rouppe van der Voort, L., Wiik, J.E., Berger, T.E.: 2005a, *Solar Phys.* **226**, 239. doi:10.1007/s11207-005-6876-3.

Lin, Y., Wiik, J.E., Engvold, O., Rouppe van der Voort, L., Frank, Z.A.: 2005b, *Solar Phys.* **227**, 283. doi:10.1007/s11207-005-1111-9.

Liu, R., Xu, Y., Wang, H.: 2010, *Mem. Soc. Astron. Ital.* **81**, 796.

Liu, W., Berger, T.E., Low, B.C.: 2012, *Astrophys. J. Lett.* **745**, L21. doi:10.1088/2041-8205/745/2/L21.

López Ariste, A., Aulanier, G., Schmieder, B., Sainz Dalda, A.: 2006, *Astron. Astrophys.* **456**, 725. doi:10.1051/0004-6361:20064923.

Mackay, D.H., Karpen, J.T., Ballester, J.L., Schmieder, B., Aulanier, G.: 2010, *Space Sci. Rev.* **151**, 333. doi:10.1007/s11214-010-9628-0.

Magara, T., Kitai, R.: 1999, *Astrophys. J.* **524**, 469. doi:10.1086/307796.

Martin, S.F.: 1973, *Solar Phys.* **31**, 3. doi:10.1007/BF00156070.

Martin, S.F.: 1990, In: Ruzdjak, V., Tandberg-Hanssen, E. (eds.) *Dynamics of Quiescent Prominences*, *IAU Colloq. 117, Lecture Notes in Physics* **363**, Springer, Berlin, 1. doi:10.1007/BFb0025641.

Martin, S.F.: 1998, *Solar Phys.* **182**, 107. doi:10.1023/A:1005026814076.

Martin, S.F.: 2003, *Adv. Space Res.* **32**, 1883. doi:10.1016/S0273-1177(03)90622-3.

Martin, S.F., Bilimoria, R., Tracadas, P.W.: 1994, In: Rutten, R.J., Schrijver, C.J. (eds.) *Solar Surface Magnetism*, Kluwer Academic, Dordrecht, 303.

Martres, M.-J., Mein, P., Schmieder, B., Soru-Escaut, I.: 1981, *Solar Phys.* **69**, 301. doi:10.1007/BF00149996.
Pesnell, W.D., Thompson, B.J., Chamberlin, P.C.: 2011, *Solar Phys.* doi:10.1007/s11207-011-9841-3.
Ridgway, C., Priest, E.R.: 1993, *Solar Phys.* **146**, 277. doi:10.1007/BF00662014.
Rondi, S., Roudier, T., Molodij, G., Bommier, V., Keil, S., Sütterlin, P., Malherbe, J.M., Meunier, N., Schmieder, B., Maloney, P.: 2007, *Astron. Astrophys.* **467**, 1289. doi:10.1051/0004-6361:20066649.
Roudier, T., Švanda, M., Meunier, N., Keil, S., Rieutord, M., Malherbe, J.M., Rondi, S., Molodij, G., Bommier, V., Schmieder, B.: 2008, *Astron. Astrophys.* **480**, 255. doi:10.1051/0004-6361:20077973.
Rutten, R.J., Bettonvil, F.C.M., Hammerschlag, R.H., Jägers, A.P.L., Leenaarts, J., Snik, F., Sütterlin, P., Tziotziou, K., de Wijn, A.G.: 2004, In: Stepanov, A.V., Benevolenskaya, E.E., Kosovichev, A.G. (eds.) *Multi-Wavelength Investigations of Solar Activity*, *IAU Symp.* **223**, 597. doi:10.1017/S1743921304006957.
Scherrer, P.H., Schou, J., Bush, R.I., Kosovichev, A.G., Bogart, R.S., Hoeksema, J.T., Liu, Y., Duvall, J.T.L., Zhao, J., Title, A.M., Schrijver, C.J., Tarbell, T.D., Tomczyk, S.: 2011, *Solar Phys.* doi:10.1007/s11207-011-9834-2.
Schmieder, B., Raadu, M.A., Wiik, J.E.: 1991, *Astron. Astrophys.* **252**, 353.
Schmieder, B., Chandra, R., Berlicki, A., Mein, P.: 2010, *Astron. Astrophys.* **514**, A68. doi:10.1051/0004-6361/200913477.
Sütterlin, P., Rutten, R.J., Skomorovsky, V.I.: 2001a, *Astron. Astrophys.* **378**, 251. doi:10.1051/0004-6361:20011176.
Sütterlin, P., Hammerschlag, R.H., Bettonvil, F.C.M., Rutten, R.J., Skomorovsky, V.I., Domyshev, G.N.: 2001b, In: Sigwarth, M. (ed.) *Advanced Solar Polarimetry — Theory, Observation, and Instrumentation*, *ASP Conf. Ser.* **236**, 431.
van Ballegooijen, A.A.: 2004, *Astrophys. J.* **612**, 519.
van Ballegooijen, A.A., Martens, P.C.H.: 1989, *Astrophys. J.* **343**, 971. doi:10.1086/167766.
Zirker, J.B., Engvold, O., Martin, S.F.: 1998, *Nature* **396**, 440. doi:10.1038/24798.